scientific reports

OPEN

Topological phase transitions without symmetry indication in NaZnSb$_{1-x}$Bi$_x$

Jaemo Jeong[1], Dongwook Kim[2] & Youngkuk Kim[1✉]

We study topological phase transitions in tetragonal NaZnSb$_{1-x}$Bi$_x$, driven by the chemical composition x. Notably, we examine mirror Chern numbers that change without symmetry indicators. First-principles calculations are performed to show that NaZnSb$_{1-x}$Bi$_x$ experiences consecutive topological phase transitions, diagnosed by the strong $\mathbb{Z}_2$ topological index ν_0 and two mirror Chern numbers μ_x and μ_{xy}. As the chemical composition x increases, the topological invariants ($\mu_x \mu_{xy} \nu_0$) change from (000), (020), (220), to (111) at $x = 0.15$, 0.20, and 0.53, respectively. A simplified low-energy effective model is developed to examine the mirror Chern number changes, highlighting the central role of spectator Dirac fermions in avoiding symmetry indicators. Our findings suggest that NaZnSb$_{1-x}$Bi$_x$ can be an exciting testbed for exploring the interplay between the topology and symmetry.

Since the discovery of archetypal topological insulators protected by time-reversal symmetry[1,2], many topological materials with potential applications have been discovered. According to the current topological materials databases[3–5], out of the 24825 materials tested, 4321 are identified as topological (crystalline) insulators, and 10007 are identified as topological semimetals. Along with topological materials, diverse topological phases have been discovered, enriched by diverse symmetries such as translation[6–9], inversion[10–14], mirror[15], rotation[16–19], or glide mirror[20–23], and with or without time-reversal symmetry[18,24–28]. Topological phases are also classified based on their order[29–32], fragility[33], delicacy[34], obstructed[35–37], and noncompact[38] atomic insulators. They are applicable with outstanding results in various apparatuses, such as chemical[39,40], electronic[27,41–44], spintronic[45–49], and quantum computer devices[50–53].

The remarkable developments in topological band theory could be one of the fundamental reasons for the success in finding topological materials and phases[54,55]. Moreover, topological quantum chemistry, or equivalently, the symmetry-based indicator method[3,56,57], has enabled efficient and high-throughput searches for topological materials. The symmetry indicator significantly simplifies the problem of identifying topological states for a given set of materials. Combined with the first-principles calculations based on density functional theory (DFT), band representations at high-symmetry momenta can efficiently indicate nontrivial band topology. Seemingly distinct topological phases are interconnected via symmetries of materials. Thus, inspecting the protecting symmetry has provided insights into determining the topological phases that share the protecting symmetries[56,58,59].

Symmetry indicators are a robust scheme, but their limitations are apparent. Notably, they fail for a specific set of topological phases, referred to as fragile topological phases[33,60], which have been a subject of intense study[61–65]. Moreover, the symmetry indicators intrinsically have a one-to-many nature[66]. Multiple stable topological phases exist for the same trivial indicator. Thus, the Berry phases and Wilson-loop calculations should be employed to determine the stable topological phase. This one-to-many nature allows for a disjointed distinction between the topological phase transitions with and without symmetry indicators. In this study, we examine a class of topological phase transitions that cannot be found in the symmetry indicators. These symmetry-uncaught topological phase transitions can occur because of the lack of symmetry to discern the topological phase transition in terms of symmetry representation[67,68]. However, the detailed process of topological phase transitions to avoid symmetry indication remains unexplored.

In this paper, we present a case study of a stable topological phase transition that occurs without symmetry indications. We perform first-principles calculations to study the topological phase transitions of NaZnSb$_{1-x}$Bi$_x$ in the presence of time-reversal symmetry driven by the chemical composition x, diagnosed by two mirror Chern numbers μ_x and μ_{xy} and the strong $\mathbb{Z}_2$ topological index ν_0. ($\mu_x \mu_{xy} \nu_0$) changes from (000), (020), (220), to (111) at $x = 0.15$, 0.20, and 0.53, respectively. Among these, the topological phase transitions from (000) to (020) and

[1]Department of Physics, Sungkyunkwan University, Suwon 16419, Korea. [2]Department of Materials Science and Engineering, University of Utah, Salt Lake City, UT 84112, USA. ✉email: youngkuk@skku.edu
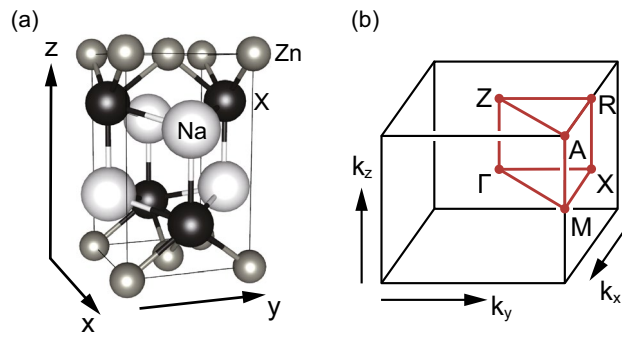
Figure 1. (**a**) Crystal structure of matlockite-type NaZnX (X = Sb and Bi) in space group $P4/nmm$ (# 129). Na, Zn, and X atoms are colored by white, grey, and black, respectively. The unit cell is represented by a solid (black) box. (**b**) Corresponding tetragonal first Brillouin zone. High-symmetry momenta are colored red.

from (020) to (220) occur within the same (trivial) symmetry indicators, thereby uncaught from the symmetry indicators. We build a simplified effective model to demonstrate a mirror Chern number change between the bands with the same symmetry representation, forbidding symmetry indication. We find that symmetry plays a role in the phase transition by providing a constraint on the positions of Dirac fermions and spectator Dirac fermions[69–71] in momentum space.

Crystal structure and symmetries. Figure 1a shows the crystal structure of NaZnX (X = Bi, Sb) in the space group $P4/nmm$ (#129). The system comprises Na-X staggered-square sublattices and Zn planar square sublattices, placed between the Na-X bilayers. The $P4/nmm$ space group has three generators - two screw rotations $\{C_{4z}|\frac{1}{2}\frac{1}{2}0\}$ and $\{C_{2x}|\frac{1}{2}\frac{1}{2}0\}$ and spatial inversion $\{\mathcal{P}|\frac{1}{2}\frac{1}{2}0\}$. C_{4z} and C_{2x} are fourfold and twofold rotations about the $\boldsymbol{z}$-axis and $\boldsymbol{x}$-axis, respectively (Fig. 1a), and $\{g|\frac{1}{2}\frac{1}{2}0\}$ ($g = C_{4z}, C_{2x}$, or $\mathcal{P}$) is a symmetry operator g followed by a fractional translation by half of the primitive unit vectors along the $\boldsymbol{x}$- and $\boldsymbol{y}$-directions. Notably, there exist x-mirror M_x and xy-glide $G_{xy} = \{M_{xy}|\frac{1}{2}\frac{1}{2}0\}$, which will be employed to evaluate the mirror Chern numbers μ_x and μ_{xy}, respectively. In addition, the system preserves time-reversal symmetry $\mathcal{T}$, enabling the $\mathbb{Z}_2$ topological insulator phase. The first Brillouin zone and the corresponding high-symmetry momenta are shown in Fig. 1b. Moreover, NaZnSb is an existing material[72–75], whereas NaZnBi is yet to be synthesized.

DFT bands. Figure 2 shows the first-principles electronic energy bands of NaZnSb$_{1-x}$Bi$_x$ calculated for various chemical compositions x using virtual crystal approximation[76,77]. A close inspection reveals that a direct bandgap exists throughout the BZ for any $x \in [0, 1]$ except for the cases where $x = 0.15$, $x = 0.20$, and $x = 0.53$. In these fine-tuned compositions, the bandgap between the conduction and valence bands vanishes such that it can form a fourfold-degenerate band crossing with linear dispersion, which is dubbed by the Dirac point. Specifically, for the case where $x = 0.15$ and $x = 0.20$, the Dirac point appears on the $\Gamma - X$ and $\Gamma - M$ lines, respectively, contained in the M_x (G_{xy}) invariant $k_x = 0$ ($k_x = -k_y$) plane. However, for $x = 0.53$, the Dirac point appears at the time-reversal invariant Γ point and mediates the band inversion between the Γ_6^+ and Γ_6^- states, as shown in Fig. 2c. The Γ_6^+ and Γ_6^- states mainly comprise the Zn s and Sb$_{1-x}$Bi$_x$ p_x and p_y orbitals, respectively, as shown in Fig. 2d For any $x \in [0, 1]$ other than these critical values, the conduction and valence bands are well separated by a direct bandgap, enabling the evaluation of the topological insulating phase from the occupied bands.

Topological phases. The Dirac points accompany a topological phase transition. Using the Wilson loop calculations[18,79,80], we enumerate two mirror Chern numbers μ_x and μ_{xy} associated with the M_x-mirror and G_{xy}-glide on the corresponding invariant planes at $k_x = 0$ and $k_x = -k_y$, respectively. (See Supplementary Information for the detailed calculations of the mirror Chern numbers). In addition, the three-dimensional strong $\mathbb{Z}_2$ topological invariant ν_0 is calculated using the parity eigenvalues of the occupied bands at eight time-reversal invariant momenta[12]. As summarized in the bottom panel of Fig. 2c, we identify the topological phases characterized by $(\mu_x, \mu_{xy}, \nu_0) = (0,0,0)$ for $0 \leq x < 0.15$, $(2,0,0)$ for $0.15 < x < 0.20$, $(2,2,0)$ for $0.20 < x < 0.53$, and $(1,1,1)$ for $0.53 < x \leq 1$. We note that the calculated $\mathbb{Z}_2$ indices for $x = 1$ are in good agreement with the previous result[81]. Correspondingly, topological phase transitions at $x = 0.15$, $x = 0.20$, and $x = 0.53$ occur owing to the changes in the mirror Chern numbers μ_x and μ_{xy} and the strong $\mathbb{Z}_2$ topological index, respectively.

For completeness, we evaluate the other possible topological crystalline phases allowed in NaZnSb$_{1-x}$Bi$_x$. First, the three-dimensional weak topological insulator phases, characterized by the three weak $\mathbb{Z}_2$ indices $(\nu_1\nu_2\nu_3)$, are turned out to be all trivial $(\nu_1\nu_2\nu_3) = (0, 0, 0)$ for all gapped phase. In addition, the $\mathbb{Z}_4$ index associated with $\mathcal{PT}$ symmetry[82], denoted by ν_4 is calculated as identical to the $\mathbb{Z}_2$ index ν_0. Thus, $\nu_4 = 0$ for $x < 0.53$ and $\nu_4 = 1$ for $x > 0.53$. Finally, the remaining topological indices are listed in Table 1. Despite the variety, the whole topological crystalline insulator phases are unambiguously determined by the weak indices and the $\mathbb{Z}_4$ index $(\nu_1, \nu_2\nu_3\nu_4)$ along with the two mirror Chern numbers μ_x and μ_{xy}[66]. The mirror Chern number μ_z is associated with the glide $g_z = \{M_z|\frac{1}{2}\frac{1}{2}0\}$ symmetry. The g_z-invariant plane $k_z = 0$ hosts four Dirac points at
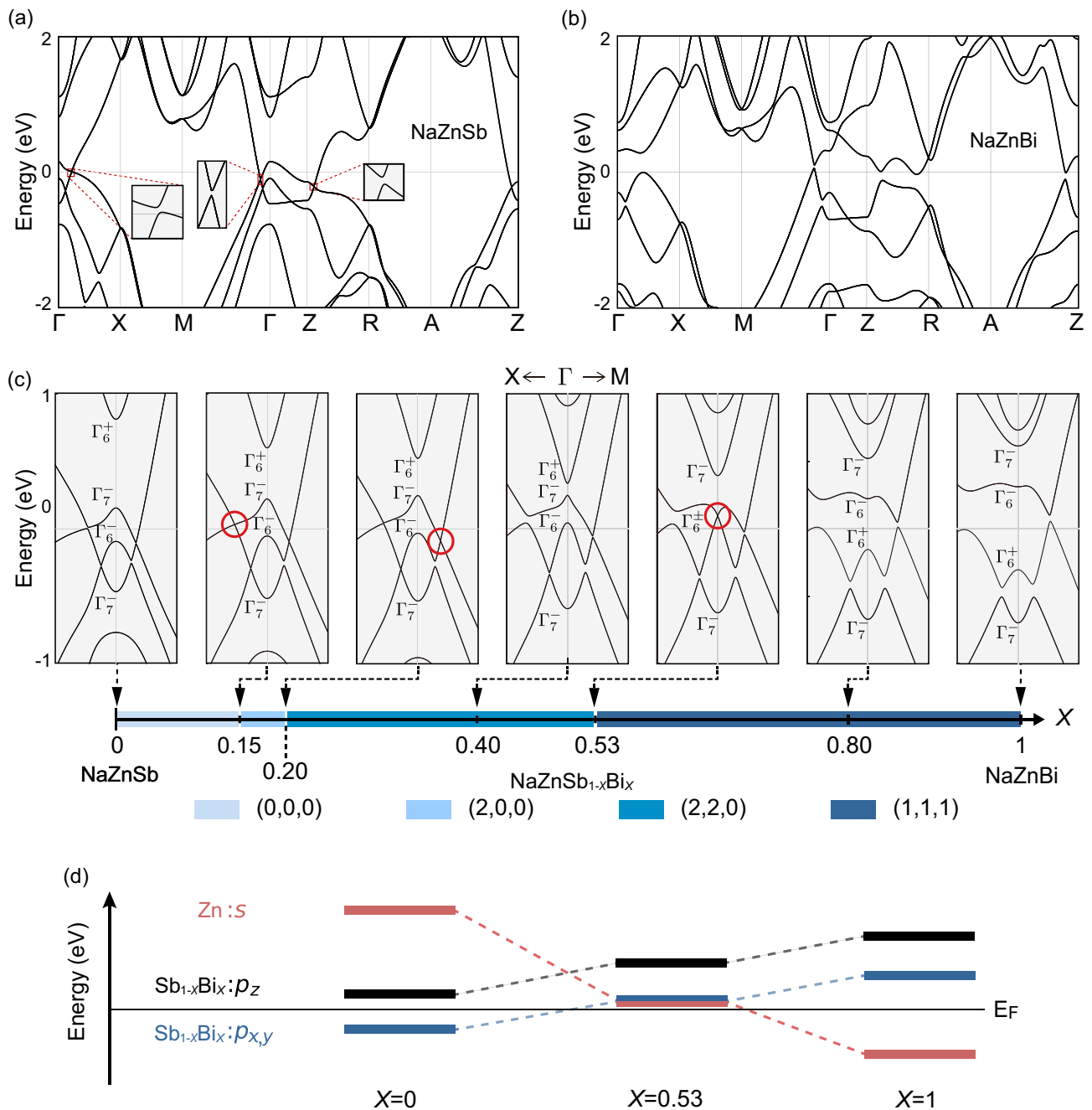
Figure 2. (**a**) First-principles bands of NaZnSb ($x = 0$) with spin-orbit coupling. The red rectangles are magnified in the guided grey boxes, showing a direct bandgap. (**b**) DFT bands of NaZnBi ($x = 1$). (**c**) DFT bands of NaZnSb$_{1-x}$Bi$_x$ for various x and topological phase diagram in x-space. The bands are drawn near the Γ point along with the X and M directions, with the corresponding chemical composition x being indicated in the topological phase diagram. The red circles in the bands highlight the massless (zero-gap) Dirac points, which appear at the topological phase boundaries. Domains in different colors indicate distinct topological phases. (**d**) Schematic diagram of the orbital characters at Γ as a function of x. The Zn-s and Sb$_{1-x}$Bi$_x$-p_x and p_y orbitals are inverted at $x = 0.53$, responsible for the change of the strong $\mathbb{Z}_2$ index.

the critical composition $x = 0.15$ and $x = 0.20$. The mirror Chern number remains trivial, $\mu_z = 0$ for $x < 0.53$, which is consistent with the symmetry constraint dictated by $\nu_4 = 0$[66].

Topological surface states. The nontrivial topology found in NaZnSb$_{1-x}$Bi$_x$ for $x > 0.15$ is demonstrated by explicit calculations of topological surface states. We prepared a slab geometry of NaZnSb$_{1-x}$Bi$_x$ comprising 15 unit cells along the [001]-direction with open boundary conditions imposed on the (001) surface. Figure 3 shows the computed surface states for (a) $x = 0.31$ and (b) $x = 1.00$, where $(\mu_x \mu_{xy} \nu_0) = (2, 2, 0)$ and $(1, 1, 1)$,
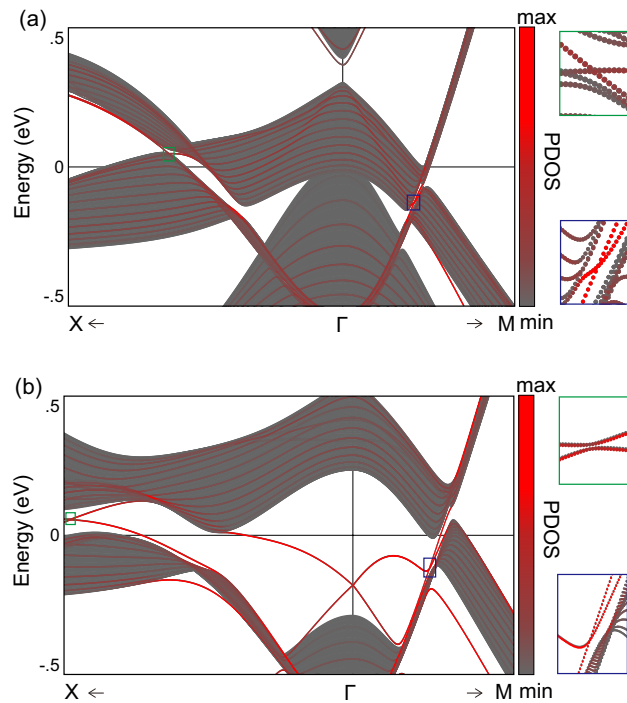
Figure 3. (001) surface energy spectra of $NaZnSb_{1-x}Bi_x$ at (**a**) $x = 0.31$ and (**b**) $x = 1.00$. The discrete energy spectra calculated from a slab geometry are overlapped with the continuous grey bulk projected spectra. The strength of the surface projection is indicated in red; the more substantial the red color, the stronger the localization at the surface. The right panels show the magnified views of the boxed regions in the left panels. The band crossing (anticrossing) is shown in the magnified views for the case of $x = 0.31$ ($x=1.00$).

respectively. When $x = 0.31$, the two surface Dirac points occur because of $\mu_x = 2$ and $\mu_{xy} = 2$ along the high-symmetry $\Gamma - X$ and $\Gamma - M$ lines of the surface BZ, respectively, where the nontrivial mirror planes are projected (Fig. 3a). For the case of $x = 1.00$, on the other hand, the strong topological insulator phase is hosted ($\nu_0 = 1$), leading to the formation of a two-dimensional surface Dirac point occurring at the surface Γ point (Fig. 3b). The calculated surface spectra agree well with the topological phases diagnosed from the bulk topological invariants.

Symmetry indicators. After identifying the topological phases of $NaZnSb_{1-x}Bi_x$, we directly evaluate the symmetry indicators, and show that the symmetry indicators proposed in this space group fail to capture the topological phase transitions at $x = 0.15$ and $x = 20$. According to Ref.[66], $NaZnSb_{1-x}Bi_x$ in space group #129 contains a set of $3\mathbb{Z}_2 \times \mathbb{Z}_4$ symmetry indicators ($\nu_1 \nu_2 \nu_3 \nu_4$). As introduced earlier, the first three indices $\nu_{i=1,2,3}$ are the three-dimensional weak $\mathbb{Z}_2$ topological indices, evaluated from the parity eigenvalues of the occupied bands[12] and the last index ν_4 is the $\mathcal{PT}$ symmetric topological invariant, evaluated from $\nu_4 \equiv \sum_{\Gamma_i \in TRIM} \frac{n_{\Gamma_i}^+ - n_{\Gamma_i}^-}{2}$ (mod 4), where $n_{\Gamma_i}^{+(-)}$ is the number of even- (odd-) parity valence bands at a time-reversal invariant momentum Γ_i[82]. From the first-principles calculations of symmetry representations, we obtain the symmetry indicators ($\nu_1 \nu_2 \nu_3 \nu_4$) = (0000) for $x < 0.53$ and (0001) for $x > 0.53$. Thus, the change in the strong index at $x = 0.53$ is captured by the symmetry indicators, but those at $x = 0.15$ and $x = 0.20$ are unseen. The absence of a symmetry indication can be attributed to the symmetry representations of the bands. Because the topological phase changes via the formation of the Dirac points that reside off the high-symmetry momenta, the symmetry representations of the bands remain the same immediately before and after the Dirac point. Therefore, the failure of the symmetry indicators is inevitable, as evaluated from the symmetry representations.

We explain the failure of symmetry indicators as being due to the so-called symmetry-allowed nature of the Chern numbers. Unlike the symmetry-protected topological phases, the Chern number characterizes a so-called symmetry-forbidden phase, in which symmetries play a role in giving rise to a constraint instead of protection. As shown by Song et al.[66], there are four varieties for a given symmetry indicator in space group #129 (See Table 1). The varieties arise from the two possibilities of the two mirror Chern numbers, that is, $\mu_i = 0, 2$ for $i = x, xy$. which are under the symmetry constraints for the two-fold C_{2i} rotation[17]

$$e^{i\pi\mu_i} = \prod_{n \in occ.} (-1)^F \prod_{\Gamma_a \in RIM} \theta_n(\Gamma_a), \qquad (1)$$

where $\theta_n(\Gamma_a) = e^{i(2J_n^a + F)\pi/2}$, J_n^a is an eigenvalue of the C_{2i} rotation for the n-th occupied band at a rotation-invariant momenta (RIM) Γ_a contained in the mirror-invariant plane, and $F = 1(0)$ for a spinful (spinless) system. Therefore, the Chern number can be changed by determining ΔC from

Space group #129 : P4/nmm								
$\mathbb{Z}_{2,2,2,4}$	$\mu_{x,0(\pi)}$	μ_{xy}	g_z	g_{xy}	c_{2z}	$c_{2x\bar{y}}$	c_{4z}	s_{2x}
0000	0 (0)	0	0	0	0	0	0	0
0000	2 (0)	0	0	0	0	0	1	1
0000	0 (0)	2	0	1	0	1	1	0
0000	2 (0)	2	0	1	0	1	0	1

Table 1. Possible topological crystalline phases corresponding to the trivial $3\mathbb{Z}_2 \times \mathbb{Z}_4$ symmetry indicators $(\nu_1\nu_2\nu_3\nu_4) = (0,0,0,0)$ in space group #129. μ_i and g_i and c_i, and s_i are the mirror and glide and rotation and screw-resolved topological invariants about the i-invariant plane and the i-axis, respectively ($i = x, xy, \cdots$). We have applied the results of Ref.[66].

$$e^{i\pi\Delta\mathcal{C}} = 1, \tag{2}$$

or equivalently,

$$\Delta\mathcal{C} = 0 \ (\text{mod } 2) \tag{3}$$

when the J_n^a remains the same before and after the variations in Chern number. Thus, $\mu_i = 0$ and $\mu_i = 2$ are symmetry-allowed, enabling the varieties of topological phases under the same symmetry structure.

Mirror-specific four-band model. We further resolve the role of symmetry in the change in mirror Chern numbers by constructing an effective Hamiltonian. Let us begin with a generic 4×4 Hamiltonian

$$\mathcal{H}(\boldsymbol{k}) = \sum_{i,j=x,y,z} h_{ij}(\boldsymbol{k})\tau_i\sigma_j, \tag{4}$$

where $\tau_{x,y,z}$ and $\sigma_{x,y,z}$ are the Pauli matrices describing the orbitals and spins, respectively. The D_{2h} point-group symmetries are distilled from the DFT bands responsible for the mirror Chern number change (See Supplementary Information for the detailed derivation of the effective model). This leads to the symmetry representations: $\mathcal{T} = i\sigma_z\mathcal{K}$, $M_{x,y,z} = i\sigma_{x,y,z}$, and $\mathcal{P} = \mathcal{I}_{4\times4}$. Here, $\mathcal{K}$ is the complex conjugation. Under the symmetry constraints

$$\mathcal{H}(\hat{O}_g\boldsymbol{k}) = U_g^\dagger\mathcal{H}(\boldsymbol{q})U_g, \tag{5}$$

where U_g and $\hat{O}_g$ are the representation for the symmetry operator g in matrix and momentum spaces, respectively, the effective Hamiltonian on the mirror-invariant plane $k_z = 0$ is obtained as

$$\mathcal{H}(\boldsymbol{k}) = A(k_x, k_y)\tau_x + B(k_x, k_y)\tau_z + C(k_x, k_y)\tau_y\sigma_z, \tag{6}$$

where $A(k_x, k_y) \equiv a_0 + a_1 k_x^2 + a_2 k_y^2$, $B(k_x, k_y) \equiv b_0 + b_1 k_x^2 + b_2 k_y^2$, and $C(k_x, k_y) \equiv c_2 k_x k_y$ to the quadratic order in $\boldsymbol{k} = (k_x, k_y)$. The corresponding energy bands are given by

$$E_\pm(\boldsymbol{k}) = \pm\sqrt{A(k_x, k_y)^2 + B(k_x, k_y)^2 + C(k_x, k_y)^2}, \tag{7}$$

for each mirror-sector $\sigma_z = \pm1$. The parameters a_i, b_i, and c_2 ($i = 0$, 1, and 2) can be fine-tuned to critical points, where $A = B = C = 0$. These conditions lead to a bandgap crossing $E_+ = E_-$ at $\boldsymbol{k} = (\pm\sqrt{-a_0/a_1}, 0)$ or $\boldsymbol{k} = (0, \pm\sqrt{-a_0/a_2})$ (We note that $c_2 = 0$ can also close band gap, but the mirror Chern number remains the same via the gap closer. See the Supplemental Information for the detailed calculations.)

The Chern number that characterizes the occupied bands $E_-(\boldsymbol{k})$ for each mirror-sectors $M_z = \pm i$ is determined by

$$\mathcal{C}_{\pm i} = \pm\left\{\text{sgn}\left[c_2\left(\frac{a_0}{a_1} - \frac{b_0}{b_1}\right)\right] - \text{sgn}\left[c_2\left(\frac{a_0}{a_2} - \frac{b_0}{b_2}\right)\right]\right\}, \tag{8}$$

from which the mirror Chern number μ_z[15,16] can be obtained as

$$\mu_z \equiv \frac{1}{2}(\mathcal{C}_{+i} - \mathcal{C}_{-i}) = \text{sgn}\left[c_2\left(\frac{a_0}{b_0} - \frac{a_2}{b_2}\right)\right] - \text{sgn}\left[c_2\left(\frac{a_0}{b_0} - \frac{a_1}{b_1}\right)\right]. \tag{9}$$

The nontrivial (trivial) topological crystalline phase indexed by $\mu_z = 2$ (=0) occurs when $(a_0 b_2 - a_2 b_0)(a_0 b_1 - a_1 b_0) < 0 (> 0)$. This equation directly shows that the bandgap crossings define the topological phase transitions between $\mu_z = 2$ and $\mu_z = 0$.

As illustrated in Fig. 4, the results of the effective model provide essential insight into the role of symmetries. The n-fold rotational symmetry generates n symmetry-related Dirac fermions whose mass is flipped simultaneously during the phase transition. This leads to variations in the Chern number with n. We believe that the fraction of n can only be changed when the symmetry is implicitly broken at the representation level, which can be deduced from the symmetry indicators. It is interesting to note the role of the spectator Dirac fermions[69,69–71], which refers to the massive Dirac fermions without mass inversion during the transition. Upon restoring a
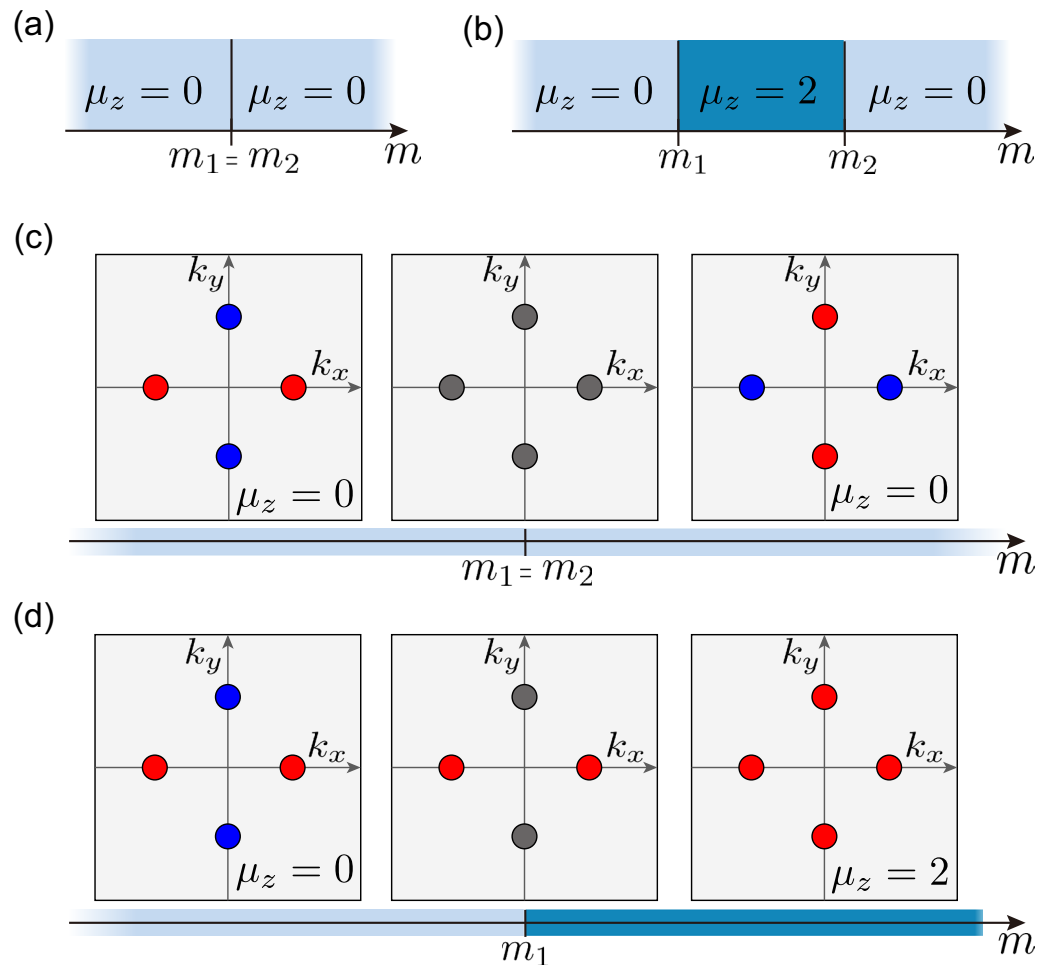
Figure 4. Schematic phase diagrams for a topological crystalline phase transition diagnosed by mirror Chern number μ_z. (**a**) Systems with C_{4z}. The Dirac and spectator Dirac points that close the band gap simultaneously at $m = m_1 = m_2$ result in the same topological crystalline phases with the mirror Chern number $\mathcal{C}_M = 0$. (**b**) Systems without C_{4z}. The Dirac and spectator Dirac points that close the band gap independently at $m = m_1$ and $m = m_2 \neq m_1$ can mediate a topological phase transition from $\mu_z = 0$ to $\mu_z = 2$. (**c**–**d**) Mass inversion of Dirac fermions in the mirror-invariant plane of momentum space: (**c**) with C_{4z} and (**d**) without C_{4z}. The red and blue circles represent the massive Dirac and the massive spectator Dirac fermions, respectively. The grey circles indicate the massless Dirac fermions.

higher-rotational symmetry, such as C_{4z}, the topological phase transition becomes trivialized by enforcing the participation of the spectator Dirac fermions. In our case, the C_{4z}-symmetry enforces $a_1 = a_2$ and $b_1 = b_2$, and thus, all the massive Dirac fermions invert the mass simultaneously to nullify the mirror Chern number change. This conforms to the symmetry constraint given by C_{4z} to the mirror Chern number. It can only change integers that are multiples of four, forbidding two. We believe that this occurs in NaZnSb$_{1-x}$Bi$_x$ at $x = 0.15$ and $x = 0.20$, where four Dirac points occur on the G_z-invariant $k_z = 0$ plane without changing the mirror Chern number $\mu_z = 0$.

Conclusions

We have performed a first-principles study on the topological phases of NaZnSb$_{1-x}$Bi$_x$ driven by the chemical composition x. We have established the topological phase diagram in x-space using symmetry indicators, two mirror Chern numbers, and the $\mathbb{Z}_2$ strong topological index. The phase boundaries are determined to be x=0.17, 0.20, and 0.53. We focused on analyzing the first two topological phase transitions, which changed the mirror Chern numbers without symmetry indications. The absence of a symmetry indication is attributed to the intrinsic nature of the Chern numbers. In general, the Chern number can jump by a factor of n without being caught by the C_n-symmetry, which can be fulfilled by hosting n massless Dirac fermions that mediate the change in the Chern number.

Our results are scientifically innovative in three aspects. First, the study provides insights into topological phase transitions, uncovering the close interplay between symmetry and topology. Second, we highlight the one-to-many nature of symmetry indicators, suggesting that materials identified as trivial in topology via symmetry inputs can be nontrivial. This may provide opportunities for finding topological materials. Finally, NaZnSb$_{1-x}$Bi$_x$

in the tetragonal phase is such an archetypal example that suggests a rich playground for exploring topological phenomena. For example, we believe that the Fermi surface topology as a function of doping concentration and chemical potential will be an interesting future study in the $NaZnSb_{1-x}Bi_x$ systems.

Methods

We performed first-principles calculations based on density functional theory (DFT) as implemented in Quantum Espresso package[83]. We used the Perdew-Burke-Ernzerhof (PBE) type general gradient approximation for exchange-correlation functional[84]. The Opium package is used to construct norm-conserving, optimized, designed non-local, and fully-relativistic pseudopotentials for the Na, Zn, Bi, and Zn atoms[85,86]. The atomic structures are fully relaxed within the force criterion of 10^{-7} eV/Å. The wave functions are expanded on a plane-wave basis with an energy cutoff of 680 eV. The atomic structures are fully relaxed within the force threshold of 10^{-5} eV/Å. The 8×8×8 sampling of the k-point grid is used based on the Monhorst-Pack scheme[87]. We have tested that this k-point grid is dense enough to achieve the self-consistent charge density and total energy convergence. Atomic substitution from Sb to Bi as a function of chemical composition x is mimicked by virtual crystal approximation[76,77]. The lattice parameters of the tetragonal unit cell are calculated as a = 4.39 Å, c = 7.36 Å for the case of X = Sb and a = 4.54 Å, c = 7.55 Å for the case of X = Bi. The unitcell comprises two formula units with six atoms Na1, Na2, Zn1, Zn2, X1, and X2 located at $(0.25a, 0.25a, 0.16c)$, $(0.75a, 0.75a, 0.84c)$, $(0.75a, 0.25a, 0.5c)$, $(0.25a, 0.75a, 0.5c)$, $(0.75a, 0.75a, 0.27c)$, and $(0.25a, 0.25a, 0.73c)$, respectively. The mirror Chern numbers[15,16] were calculated using the mirror-specified Wilson loop calculations[18,78–80]. The Wilson Hamiltonians are generated by the Soluyanov and Vanderbilt method[88], using the Pw2wan utility in Wannier90 code[89–93].

Data availability

The datasets generated from the current study are available from the corresponding author upon reasonable request.

References

1. Hasan, M. Z. & Kane, C. L. Colloquium: Topological insulators. *Rev. Mod. Phys.* **82**, 3045 (2010).
2. Qi, X.-L. & Zhang, S.-C. Topological insulators and superconductors. *Rev. Mod. Phys.* **83**, 1057 (2011).
3. Bradlyn, B. *et al.* Topological quantum chemistry. *Nature* **547**, 298 (2017).
4. Vergniory, M. *et al.* A complete catalogue of high-quality topological materials. *Nature* **566**, 480 (2019).
5. Vergniory, M. G., Wieder, B. J., Elcoro, L., Parkin, S. S., Felser, C., Bernevig, B. A. & Regnault, N. All topological bands of all stoichiometric materials. arXiv preprint arXiv:2105.09954 (2021).
6. Fu, L., Kane, C. L. & Mele, E. J. Topological insulators in three dimensions. *Phys. Rev. Lett.* **98**, 106803 (2007).
7. Moore, J. E. & Balents, L. Topological invariants of time-reversal-invariant band structures. *Phys. Rev. B* **75**, 121306 (2007).
8. Cheng, M., Zaletel, M., Barkeshli, M., Vishwanath, A. & Bonderson, P. Translational symmetry and microscopic constraints on symmetry-enriched topological phases: A view from the surface. *Phys. Rev. X* **6**, 041068 (2016).
9. Song, H., Huang, S.-J., Fu, L. & Hermele, M. Topological phases protected by point group symmetry. *Phys. Rev. X* **7**, 011020 (2017).
10. Turner, A. M., Zhang, Y. & Vishwanath, A. Entanglement and inversion symmetry in topological insulators. *Phys. Rev. B* **82**, 241102 (2010).
11. Hughes, T. L., Prodan, E. & Bernevig, B. A. Inversion-symmetric topological insulators. *Phys. Rev. B* **83**, 245132 (2011).
12. Fu, L. & Kane, C. L. Topological insulators with inversion symmetry. *Phys. Rev. B* **76**, 045302 (2007).
13. Ahn, J., Kim, D., Kim, Y. & Yang, B.-J. Band topology and linking structure of nodal line semimetals with Z^2 monopole charges. *Phys. Rev. Lett.* **121**, 106403 (2018).
14. Jeon, S. & Kim, Y. Two-dimensional weak topological insulators in inversion-symmetric crystals. *Phys. Rev. B* **105**, L121101 (2022).
15. Teo, J. C. Y., Fu, L. & Kane, C. L. Surface states and topological invariants in three-dimensional topological insulators: Application to $bi_{1-x}sb_x$. *Phys. Rev. B* **78**, 045426 (2008).
16. Fu, L. Topological crystalline insulators. *Phys. Rev. Lett.* **106**, 106802 (2011).
17. Fang, C., Gilbert, M. J., Dai, X. & Bernevig, B. A. Multi-Weyl topological semimetals stabilized by point group symmetry. *Phys. Rev. Lett.* **108**, 266802 (2012).
18. Alexandradinata, A., Fang, C., Gilbert, M. J. & Bernevig, B. A. Spin-orbit-free topological insulators without time-reversal symmetry. *Phys. Rev. Lett.* **113**, 116403 (2014).
19. Fang, C. & Fu, L. New classes of topological crystalline insulators having surface rotation anomaly. *Sci. Adv.* **5**, eaat2374 (2019).
20. Young, S. M. & Kane, C. L. Dirac semimetals in two dimensions. *Phys. Rev. Lett.* **115**, 126803 (2015).
21. Fang, C. & Fu, L. New classes of three-dimensional topological crystalline insulators: Nonsymmorphic and magnetic. *Phys. Rev. B* **91**, 161105 (2015).
22. Wang, Z., Alexandradinata, A., Cava, R. J. & Bernevig, B. A. Hourglass fermions. *Nature* **532**, 189 (2016).
23. Wieder, B. J. *et al.* Wallpaper fermions and the nonsymmorphic Dirac insulator. *Science* **361**, 246 (2018).
24. Li, R., Wang, J., Qi, X.-L. & Zhang, S.-C. Dynamical axion field in topological magnetic insulators. *Nat. Phys.* **6**, 284 (2010).
25. Burkov, A. A., Hook, M. D. & Balents, L. Topological nodal semimetals. *Phys. Rev. B* **84**, 235126 (2011).
26. Bonderson, P., Nayak, C. & Qi, X.-L. A time-reversal invariant topological phase at the surface of a 3d topological insulator. *J. Stat. Mech. Theory Exp.* **2013**, P09016 (2013).
27. Tokura, Y., Yasuda, K. & Tsukazaki, A. Magnetic topological insulators. *Nat. Rev. Phys.* **1**, 126 (2019).
28. Elcoro, L. *et al.* Magnetic topological quantum chemistry. *Nat. Commun.* **12**, 1 (2021).
29. Benalcazar, W. A., Bernevig, B. A. & Hughes, T. L. Quantized electric multipole insulators. *Science* **357**, 61 (2017).
30. Schindler, F. *et al.* Higher-order topological insulators. *Science advances* **4**, eaat0346 (2018).
31. Khalaf, E. Higher-order topological insulators and superconductors protected by inversion symmetry. *Phys. Rev. B* **97**, 205136 (2018).
32. Călugăru, D., Juričić, V. & Roy, B. Higher-order topological phases: A general principle of construction. *Phys. Rev. B* **99**, 041301 (2019).
33. Po, H. C., Watanabe, H. & Vishwanath, A. Fragile topology and Wannier obstructions. *Phys. Rev. Lett.* **121**, 126402 (2018).
34. Nelson, A., Neupert, T., Bzdušek, T. C. V. & Alexandradinata, A. Multicellularity of delicate topological insulators. *Phys. Rev. Lett.* **126**, 216404 (2021).

35. Cano, J. *et al.* Building blocks of topological quantum chemistry: Elementary band representations. *Phys. Rev. B* **97**, 035139 (2018).
36. Xu, Y., Elcoro, L., Song, Z.-D., Vergniory, M. G., Felser, C., Parkin, S. S. P., Regnault, N., Mañes, J. L. & Bernevig, B. A. Filling-enforced obstructed atomic insulators. arXiv:2106.10276 (2021).
37. Cano, J., Elcoro, L., Aroyo, M. I., Bernevig, B. A. & Bradlyn, B. Topology invisible to eigenvalues in obstructed atomic insulators. *Phys. Rev. B* **105**, 125115 (2022).
38. Schindler, F. & Bernevig, B. A. Noncompact atomic insulators. *Phys. Rev. B* **104**, L201114 (2021).
39. Sattigeri, R. M., Jha, P. K., Śpiewak, P. & Kurzydłowski, K. J. Two dimensional limgas; a novel topological quantum catalyst for hydrogen evolution reaction. arXiv preprint arXiv:2204.08926 (2022)
40. Kim, D. & Liu, F. Topological alloy engineering and locally linearized gap dependence on concentration. *Phys. Rev. B* **106**, 085105 (2022).
41. Sacépé, B. *et al.* Gate-tuned normal and superconducting transport at the surface of a topological insulator. *Nat. Commun.* **2**, 1 (2011).
42. Steinberg, H., Laloë, J.-B., Fatemi, V., Moodera, J. S. & Jarillo-Herrero, P. Electrically tunable surface-to-bulk coherent coupling in topological insulator thin films. *Phys. Rev. B* **84**, 233101 (2011).
43. Kong, D. *et al.* Ambipolar field effect in the ternary topological insulator (bixsb1-x) 2te3 by composition tuning. *Nat. Nanotechnol.* **6**, 705 (2011).
44. Dhori, B. R., Sattigeri, R. M., Jha, P. K., Kurzydlowski, D. & Chakraborty, B. A first-principles investigation of pressure induced topological phase transitions in half-Heusler AgSrBi. *Mater. Adv.* **3**, 3938 (2022).
45. Hsieh, D. *et al.* A topological Dirac insulator in a quantum spin hall phase. *Nature* **452**, 970 (2008).
46. Zhang, H. *et al.* Topological insulators in bi2se3, bi2te3 and sb2te3 with a single Dirac cone on the surface. *Nat. Phys.* **5**, 438 (2009).
47. Chen, Y. L. *et al.* Experimental realization of a three-dimensional topological insulator Bi_2Te_3. *Science* **325**, 178 (2009).
48. Garate, I. & Franz, M. Inverse spin-galvanic effect in the interface between a topological insulator and a ferromagnet. *Phys. Rev. Lett.* **104**, 146802 (2010).
49. He, M., Sun, H. & He, Q. L. Topological insulator: Spintronics and quantum computations. *Front. Phys.* **14**, 1 (2019).
50. Freedman, M. H., Larsen, M. & Wang, Z. A modular functor which is universalʕ for quantum computation. *Commun. Math. Phys.* **227**, 605 (2002).
51. Das Sarma, S., Nayak, C. & Tewari, S. Proposal to stabilize and detect half-quantum vortices in strontium ruthenate thin films: Non-abelian braiding statistics of vortices in a $p_x + ip_y$ superconductor. *Phys. Rev. B* **73**, 220502 (2006).
52. Nayak, C., Simon, S. H., Stern, A., Freedman, M. & Das Sarma, S. Non-abelian anyons and topological quantum computation. *Rev. Mod. Phys.* **80**, 1083 (2008).
53. Checkelsky, J. G., Ye, J., Onose, Y., Iwasa, Y. & Tokura, Y. Dirac-fermion-mediated ferromagnetism in a topological insulator. *Nat. Phys.* **8**, 729 (2012).
54. Kane, C. L. Topological band theory and the Z_2 invariant. In *Contemporary Concepts of Condensed Matter Science* Vol. 6 3–34 (Elsevier, 2013).
55. Bansil, A., Lin, H. & Das, T. Colloquium: Topological band theory. *Rev. Mod. Phys.* **88**, 021004 (2016).
56. Kruthoff, J., de Boer, J., van Wezel, J., Kane, C. L. & Slager, R.-J. Topological classification of crystalline insulators through band structure combinatorics. *Phys. Rev. X* **7**, 041069 (2017).
57. Po, H. C., Vishwanath, A. & Watanabe, H. Complete theory of symmetry-based indicators of band topology. *Nat. Commun.* **8**, 50 (2017).
58. Zak, J. Band representations of space groups. *Phys. Rev. B* **26**, 3010 (1982).
59. Serbyn, M. & Fu, L. Symmetry breaking and landau quantization in topological crystalline insulators. *Phys. Rev. B* **90**, 035402 (2014).
60. Bouhon, A., Black-Schaffer, A. M. & Slager, R.-J. Wilson loop approach to fragile topology of split elementary band representations and topological crystalline insulators with time-reversal symmetry. *Phys. Rev. B* **100**, 195135 (2019).
61. Kooi, S. H., van Miert, G. & Ortix, C. Classification of crystalline insulators without symmetry indicators: Atomic and fragile topological phases in twofold rotation symmetric systems. *Phys. Rev. B* **100**, 115160 (2019).
62. Hwang, Y., Ahn, J. & Yang, B.-J. Fragile topology protected by inversion symmetry: Diagnosis, bulk-boundary correspondence, and Wilson loop. *Phys. Rev. B* **100**, 205126 (2019).
63. Song, Z.-D., Elcoro, L., Xu, Y.-F., Regnault, N. & Bernevig, B. A. Fragile phases as affine monoids: Classification and material examples. *Phys. Rev. X* **10**, 031001 (2020).
64. Song, Z.-D., Elcoro, L. & Bernevig, B. A. Twisted bulk-boundary correspondence of fragile topology. *Science* **367**, 794 (2020).
65. Peri, V. *et al.* Experimental characterization of fragile topology in an acoustic metamaterial. *Science* **367**, 797 (2020).
66. Song, Z., Zhang, T., Fang, Z. & Fang, C. Quantitative mappings between symmetry and topology in solids. *Nat. Commun.* **9**, 3530 (2018).
67. Zhou, X. *et al.* Topological crystalline insulator states in the Ca2As family. *Phys. Rev. B* **98**, 241104 (2018).
68. Hsu, C.-H. *et al.* Purely rotational symmetry-protected topological crystalline insulator-Bi4Br4. *2D Mater.* **6**, 031004 (2019).
69. Haldane, F. D. M. Model for a quantum hall effect without landau levels: Condensed-matter realization of the "parity anomaly". *Phys. Rev. Lett.* **61**, 2015 (1988).
70. Hatsugai, Y., Kohmoto, M. & Wu, Y.-S. Hidden massive Dirac fermions in effective field theory for integral quantum hall transitions. *Phys. Rev. B* **54**, 4898 (1996).
71. Watanabe, H., Hatsugai, Y. & Aoki, H. Half-integer contributions to the quantum hall conductivity from single Dirac cones. *Phys. Rev. B* **82**, 241403 (2010).
72. Jain, A. *et al.* The Materials Project: A materials genome approach to accelerating materials innovation. *APL Mater.* **1**, 011002 (2013).
73. Jaiganesh, G., Britto, T. M., Eithiraj, R. D. & Kalpana, G. Electronic and structural properties of NaZnx (x= p, as, sb): an ab initio study. *J. Phys. Condes. Matter* **20**, 085220 (2008).
74. Savelsberg, G. & Schaefer, H. Ternaere pnictide und chalkogenide von alkalimetallen und IB-bzw. IIB-elementen. *Z. Naturforsch. B* **33**, 370 (1978).
75. Kahlert, H. & Schuster, H.-U. Ternary phases of sodium or potassium with elements of the 2 b- and 5 b-group. *Z. Naturforsch. B* **31**, 1538 (1976).
76. Nordheim, L. Zur elektronentheorie der metalle. I. *Ann. Phys.* **401**, 607 (1931).
77. Bellaiche, L. & Vanderbilt, D. Virtual crystal approximation revisited: Application to dielectric and piezoelectric properties of perovskites. *Phys. Rev. B* **61**, 7877 (2000).
78. Alexandradinata, A., Dai, X. & Bernevig, B. A. Wilson-loop characterization of inversion-symmetric topological insulators. *Phys. Rev. B* **89**, 155114 (2014).
79. Alexandradinata, A. & Bernevig, B. A. Berry-phase description of topological crystalline insulators. *Phys. Rev. B* **93**, 205104 (2016).
80. Alexandradinata, A., Wang, Z. & Bernevig, B. A. Topological insulators from group cohomology. *Phys. Rev. X* **6**, 021008 (2016).
81. Lee, H., Kang, Y.-G., Jung, M.-C., Han, M. J. & Chang, K. J. Robust dual topological insulator phase in NaZnBi. *NPG Asia Mater.* **14**, 1 (2022).
82. Khalaf, E., Po, H. C., Vishwanath, A. & Watanabe, H. Symmetry indicators and anomalous surface states of topological crystalline insulators. *Phys. Rev. X* **8**, 031070 (2018).

8

83. Giannozzi, P. *et al.* Quantum espresso: A modular and open-source software project for quantum simulations of materials. *J. Phys. Condens. Matter* **21**, 395502 (2009).
84. Perdew, J. P., Burke, K. & Enzerhof, M. Generalized gradient approximation made simple. *Phys. Rev. Lett.* **77**, 3865 (1996).
85. Rappe, A. M., Rabe, K. M., Kaxiras, E. & Joannopoulos, J. D. Optimized pseudopotentials. *Phys. Rev. B* **41**, 1227 (1990).
86. Ramer, N. J. & Rappe, A. M. Designed nonlocal pseudopotentials for enhanced transferability. *Phys. Rev. B* **59**, 12471 (1999).
87. Monkhorst, H. J. & Pack, J. D. Special points for Brillouin-zone integrations. *Phys. Rev. B* **13**, 5188 (1976).
88. Soluyanov, A. A. & Vanderbilt, D. Wannier representation of z_2 topological insulators. *Phys. Rev. B* **83**, 035108 (2011).
89. Marzari, N. & Vanderbilt, D. Maximally localized generalized Wannier functions for composite energy bands. *Phys. Rev. B* **56**, 12847 (1997).
90. Souza, I., Marzari, N. & Vanderbilt, D. Maximally localized Wannier functions for entangled energy bands. *Phys. Rev. B* **65**, 035109 (2001).
91. Mostofi, A. A. *et al.* wannier90: A tool for obtaining maximally-localised Wannier functions. *Comput. Phys. Commun.* **178**, 685 (2008).
92. Taherinejad, M., Garrity, K. F. & Vanderbilt, D. Wannier center sheets in topological insulators. *Phys. Rev. B* **89**, 115102 (2014).
93. Marzari, N., Mostofi, A. A., Yates, J. R., Souza, I. & Vanderbilt, D. Maximally localized Wannier functions: Theory and applications. *Rev. Mod. Phys.* **84**, 1419 (2012).

Acknowledgements

Author contributions

Y.K. conceived the idea and organized the research. J.J. and Y.K carried out first-principles calculations and the k.p model calculations. D.K. and Y.K. diagnosed the topological phases and developed the low-energy effective Hamiltonian. J.J. and Y.K. wrote the manuscript. All authors discussed the results.

Competing Interests

The authors declare no competing interests.

Additional information

Supplementary Information The online version contains supplementary material available at https://doi.org/10.1038/s41598-022-26596-y.

Correspondence and requests for materials should be addressed to Y.K.

Reprints and permissions information is available at www.nature.com/reprints.

Publisher's note Springer Nature remains neutral with regard to jurisdictional claims in published maps and institutional affiliations.